# Formation and relaxation of coherency strain in the nickel-base superalloy SC16

**Haroldo Cavalcanti Pinto and Giovanni Bruno*†**

*Hahn-Meitner Institut, Glienicker Straße 100, D-14109 Berlin, Germany. E-mail: bruno@ill.fr*

An *in situ* study of the kinetics of relaxation of the $\gamma$–$\gamma'$ lattice mismatch in the single-crystal Ni-base superalloy SC16 was carried out by means of high-energy synchrotron radiation diffraction. The high resolution achievable was exploited to measure the time variation of the $\gamma$ and $\gamma'$ lattice parameters during isothermal ageing at several temperatures, starting from the $\gamma'$ solvus point. On cooling from the solvus temperature (1523 K) the $\gamma'$ precipitate phase nucleates and grows following concurrent mechanisms. The variations of the $\gamma$ and $\gamma'$ peak position and integrated intensity could be followed by means of fundamental and superstructure reflections. At each temperature $T < 1473$ K the integrated intensity follows an Avrami time law. The $\gamma'$ volume fraction increases as a function of time at each temperature. It increases with cooling, until saturation occurs at temperatures as low as 1075 K. The lattice mismatch follows an exponential time decay, while having larger values at high temperatures. The particles are born fully coherent, and the coherency strains the set-up. Over time, long-term ageing shows a stabilization of the misfit value, while the precipitates are supposed to lose their coherency to the matrix (within 3–4 h) and the strains relax.

**Keywords: nickel superalloys; misfit; coherency strains; *in situ* X-ray diffraction; high resolution.**

## 1. Introduction

Nickel-base superalloys find their application in turbine blades for power generation and for the aircraft industry (MacKay & Nathal, 1986). The superalloy SC16 was one of the first of the single-crystal materials developed in the 1970s. Its composition is given in Table 1. The cube-shaped $\gamma'$ particles are periodically arranged and oriented with the edges along the ⟨100⟩ directions. Their average size lies around 300–400 nm, whereas the channel width is about 70 nm.

The alloy SC16 has a relatively low $\gamma'$ volume fraction (about 40%). Although alloys that contain heavy refractory elements have been developed more recently, the low number of compositional elements in SC16 allows the diffusion properties to be modelled more easily. Furthermore, the width of the $\gamma$-channels is larger (60–100 nm) than for new superalloys (∼10–20 nm), which possess a high $\gamma'$ volume fraction (70–80%). Therefore, in SC16 the relaxation of the $\gamma$ lattice parameter far from the coherent $\gamma$–$\gamma'$ interface is easier to observe.

A macroscopic structure overlaps the 'paving stones' (the $\gamma'$ particles): during the growth of the as-cast ingot, some elements (typically Cr and Al) segregate into a dendritic structure, which extends along the crystallographic ⟨100⟩ directions. The $\gamma'$ size and shape vary considerably from dendrites to interdendritic regions (Fig. 1). The peculiar mechanical and physical properties of these alloys can be achieved by means of a 'standard heat treatment', SHT (Malow *et al.*, 1994). In the alloy SC16 this treatment consists of a homogenization at 1523 K (usually for 3 h), ageing at 1373 K for 4 h and final stabilization with an ageing treatment for 24 h at 1123 K.

**Table 1**
Composition of the SC16 superalloy.

| Element | Ni | Al | Ti | Ta | Cr | Mo |
|---|---|---|---|---|---|---|
| %at | 68.1 | 7.35 | 4.15 | 1.1 | 17.5 | 1.8 |

The precipitate phase $\gamma'$ has an f.c.c. crystal structure, which is similar to the $\gamma$ matrix but has chemical $Ni_3$(Al, Ti, Ta) order ($L1_2$ structure). The two phases $\gamma$ and $\gamma'$ have slightly different lattice parameters $a_\gamma$ and $a_{\gamma'}$, so that it is convenient to define the $\gamma$–$\gamma'$ lattice mismatch as (MacKay & Nathal, 1986)

$$\delta = 2(a_{\gamma'} - a_\gamma)/(a_{\gamma'} + a_\gamma). \quad (1)$$

The evolution of the misfit $\delta$ is important for two reasons:

(i) Technologically speaking, the heat treatments applied prior to industrial applications can be optimized only with detailed knowledge of the evolution of the alloy parameters with time and temperature.

(ii) From a metallurgical point of view, it is important to know how the nucleation and stabilization of the $\gamma'$ phase occur. Three driving mechanisms rule these kinetics (Haasen, 1993): the interfacial energy $\sigma_{\gamma\gamma'}$, the coherency energy $E_\delta$ and the Helmoltz free energy of $\gamma'$

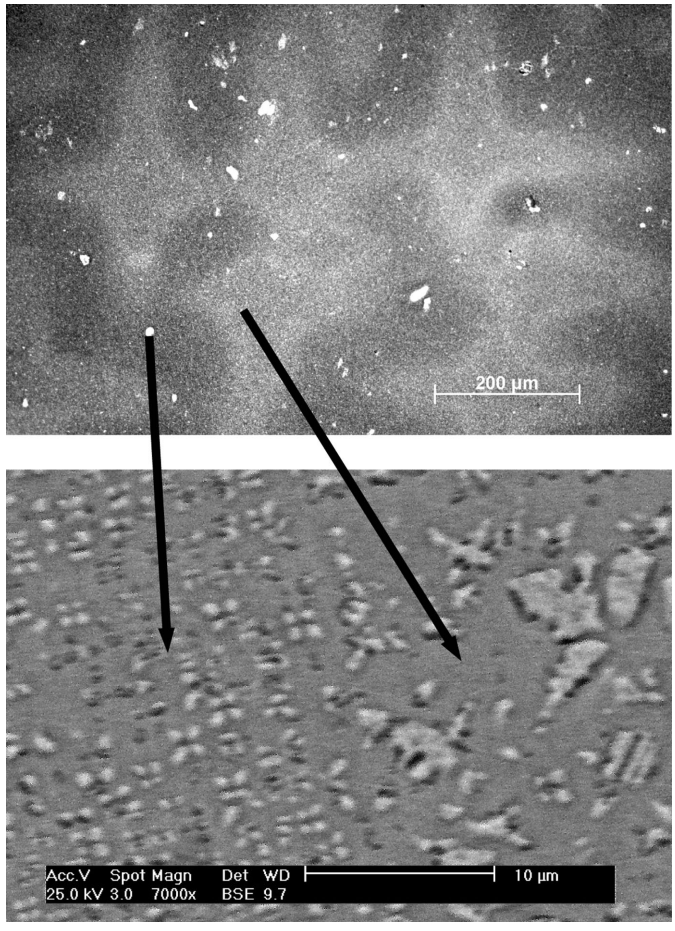


**Figure 1**
Macroscopic dendritic structure (*a*) and microscopic implications (*b*). In the interdendritic zones the particles become larger, their shape is less regular and they are more disordered than particles in the dendritic zones. The density of pores is higher in the interdendritic regions.

† Current address: Institute Laue Langevin, 6 rue Horowitz, F-38042 Grenoble CEDEX 9, France.

  

nucleation $F_{\gamma'}$. The last two contributions are temperature dependent and their relative weight turns the reaction into 'surface' or 'strain' driven: the prevalence of one of the terms changes drastically the shape and the size of the precipitates. Thus, the lattice mismatch between the matrix $\gamma$ and the precipitates $\gamma'$, and the coherency strains between the two phases, strongly influence the structural evolution of the alloy with temperature.

In addition, the value of the misfit at high temperature directly influences the creep behaviour, as reported by Fredholm & Strudel (1984). Thus, the evolution of $\delta$ as a function of time and temperature directly relates to the evolution of creep during service conditions.

Very few *in situ* investigations that follow the $\gamma'$ particle nucleation and growth are available. Some authors have performed TEM (Malow *et al.*, 1994; Hopgood & Martin, 1986; Malow, 1993) on quenched samples, while other authors have used synchrotron radiation diffraction. The latters started from the SHT condition and heated up to 1473 K (Royer *et al.*, 1997, 1998). Bruno & Pinto (2003) attempted to study the early stages of $\gamma'$ nucleation and growth by means of neutron diffraction. None of the quoted works attempt to follow the evolution of the mismatch as a function of time.

The intensity and resolution achievable at a synchrotron beamline are at least one order of magnitude higher than the most advanced laboratory method, *e.g.* convergent-beam electron diffraction (CBED). The availability of high-temperature furnaces also allows *in situ* experiments, which are at least problematic for other techniques (Bruno, Schumacher *et al.*, 2003). The present work describes the real-time evolution of the lattice mismatch at several temperatures; we start from the solutionized state (*i.e.* cooling from the solvus temperature $T = 1523$ K). Stabilization and relaxation of the coherency strains in long ageing treatments are observed. This opens the possibilities of future *in situ* investigations in industrial on-line process control.

## 2. Experimental methods

Several successive isothermal ageings were applied, using a sawtooth temperature profile (Fig. 2). Longer ageing times were used at 1273 K and 1123 K. An analagous approach has been successfully used by Bruno & Pinto (2003) and Bruno, Pinto *et al.* (2003), where the maximum of the reaction rate for $\gamma'$ nucleation and growth was found to be around 1273–1323 K. Bruno, Pinto *et al.* (2003) also observed a dramatic change in the particle arrangement and size distribution. The reason for the long ageing at 1123 K will be seen later. A high-temperature mirror furnace, which is able to reach 1773 K with a temperature homogeneity of about $\pm 10$ K in a volume of about $10 \times 10 \times 10$ mm at the sample position (Lorenz *et al.*, 1993), was used for all *in situ* investigations. The sample temperature was monitored by a Pt–PtRh thermocouple, which served as input for the controller. The Eurotherm controller allowed a fine-temperature tuning (up to $\pm 3$ K), in a very short time (about 2 min), so that the largest source of error in the temperature determination came from the inhomogeneity of the focusing region. The thermocouple was fitted into a shallow hole drilled in the sample itself by spark erosion; thus thermal contact was ensured.

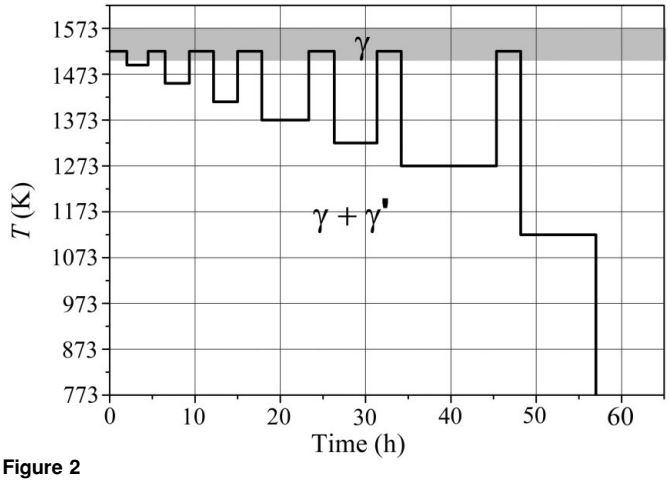


**Figure 2**
Typical schematic sample temperature profile during the real-time diffraction measurements. The pure $\gamma$ region is sketched, for the sake of clarity, above $T_c = 1473$ K, but $\gamma'$ also starts forming at around 1493 K. Longer ageing times were chosen at 1273 K and 1123 K (profile not shown).

Synchrotron radiation diffraction measurements were performed on the high-energy beamline BW5 of the HASYLAB facility at DESY, Hamburg, Germany (Bouchard *et al.*, 1998). On BW5, a 'three crystal' configuration was used, with an Si(220) perfect monochromator and analyser. The wavelength used was $\lambda = 0.11294$ Å (which corresponds to an energy of $E = 109.8$ keV) and all measurements were performed in the so-called (+, −, +) mode (Rütt *et al.*, 1995). A beam size of $3 \times 3$ mm was preferred in order to reduce the data-acquisition time. Nevertheless, to acquire peaks with sufficient resolution ($2\theta$ step of down to $2.5 \times 10^{-4}$ deg), a total counting time of about 5 min was required for each peak.

Three other samples were investigated on the beamline PETRA II at HASYLAB, Hamburg (Kampmann *et al.*, 2001), with a similar experimental arrangement, since the two beamlines share the same general layout. These samples were pre-aged at 1273 K for 25 h and 100 h and at 1123 K for 150 h (and suddenly quenched to freeze their microstructure). Samples of size $5 \times 5 \times 8$ mm were cut from the same single-crystal ingot. They were previously oriented in a Laue Camera, with faces parallel to the {100} lattice planes.

## 3. Results

The typical order of magnitude of $\delta$ is about $10^{-3}$ Å. Therefore, the separation of the $\gamma$ and $\gamma'$ peaks would require a resolution of about $5 \times 10^{-4}$ Å. This is impossible, for example, at a neutron source if we want to maintain limited counting times. Therefore, Bruno & Pinto (2003) were only able to follow the time and temperature evolution of the $\gamma'$ volume fraction by monitoring the superstructure reflections. On BW5 the resolution, as measured with a perfect Si(220) single crystal at the sample position, easily reached $1 \times 10^{-4}$ Å. This allowed us not only to record the $\gamma$ and $\gamma'$ peak positions but also to see the further peak splitting due to the dendritic structure typical of these alloys. The variety of particle 'zoology' is shown in Fig. 1, and the corresponding diffraction patterns are displayed in Fig. 3.

The presence of extra peaks, which come from interdendritic structures, from the $\gamma'$ 'depletion regions' around the precipitates and from the different strain fields around particles of different size and shape, considerably complicates the data analysis. The dendrites are supposed to be present even at very high temperature, because they stem from the alloy-ingot growth itself. The $\gamma'$ depletion regions are supposed to form during the nucleation and subsequent growth, because of local diffusion phenomena at the $\gamma$–$\gamma'$ interface (Johnson *et al.*, 1990). The different strain fields are caused simply by the different extent of the coherency effect between matrix and precipitates, which of course depend on the $\gamma'$ size.

Examples of the 200 peak obtained at various temperatures are shown in Fig. 3. At very high temperatures (1493 K, Fig. 3*a*) the $\gamma'$ phase has a tiny volume fraction, whereas at lower $T$ (1373 K and 1323 K, Figs. 3*b* and 3*c*) the $\gamma'$ phase rises to about 20–25% and

shows extra peaks. The matrix phase shows, at every temperature, the presence of two or three sub-peaks near the main peak.

The necessity of using a fine step-scan to reveal all the details of the diffraction patterns, keeping counting times low, obliged us to use only the fundamental reflection 200 at high temperatures. The superstructure reflection 100 was mapped at room temperature and on the three pre-aged samples mentioned above. The measurements on the 100 reflection were possible because the kinetics are much slower at very long ageing times. Examples of the contour plots, *i.e.* reciprocal space mappings in the $\omega$–$2\theta$ coordinate system on the samples aged at 1273 K for 100 h and 1123 K for 150 h, are shown in Figs. 4(*a*) and 4(*b*) for the 100 reflection and in Figs. 4(*c*) and 4(*d*) for the 200 reflection. The high resolution allows us to build a very detailed picture of the crystal mosaic structure. The superstructure reflection essentially does not change its character with temperature and two main sub-grains are visible. In Fig. 4(*b*) the sample is rotated 180° in $\chi$, so that the $\omega$ scale is reversed. The fundamental reflection shows the presence of three sub-grains. The $\omega$ range scanned in this case is in fact larger. Figs. 4(*c*) and 4(*d*) show that the $\gamma$ peak becomes narrower as the temperature decreases. This is in agreement with the results found by Bruno, Schumacher *et al.* (2003), where the $\gamma$ phase always has a larger FWHM than $\gamma'$, except where $\delta$ goes to 0 around $T = 773$ K.

The results of the real-time measurements are shown in Figs. 5 and 6. The intensity of the two main peaks follows a specular behaviour, as is to be expected. While the $\gamma'$ phase grows, the $\gamma$ phase volume fraction decreases. In Fig. 5 the total sum of the intensities was normalized to 1. However, only the main peaks, visible in Figs. 3(*a*)–3(*c*), were taken into account in the intensity- and lattice-parameter calculations. The presence of sub-peaks was basically neglected, because they have a very small integrated intensity and their origin is not clear. In fact, it can be reckoned that $\gamma'$-depleted matrix regions and interdendritic areas can bring about additional diffraction contributions. The precipitation of TCP (topologically close packed) phases, as reported by Gilles *et al.* (1997) and Durand-Charre (1997), can also cause extra peaks. The results of the lattice mismatch calculations are shown in Fig. 6.

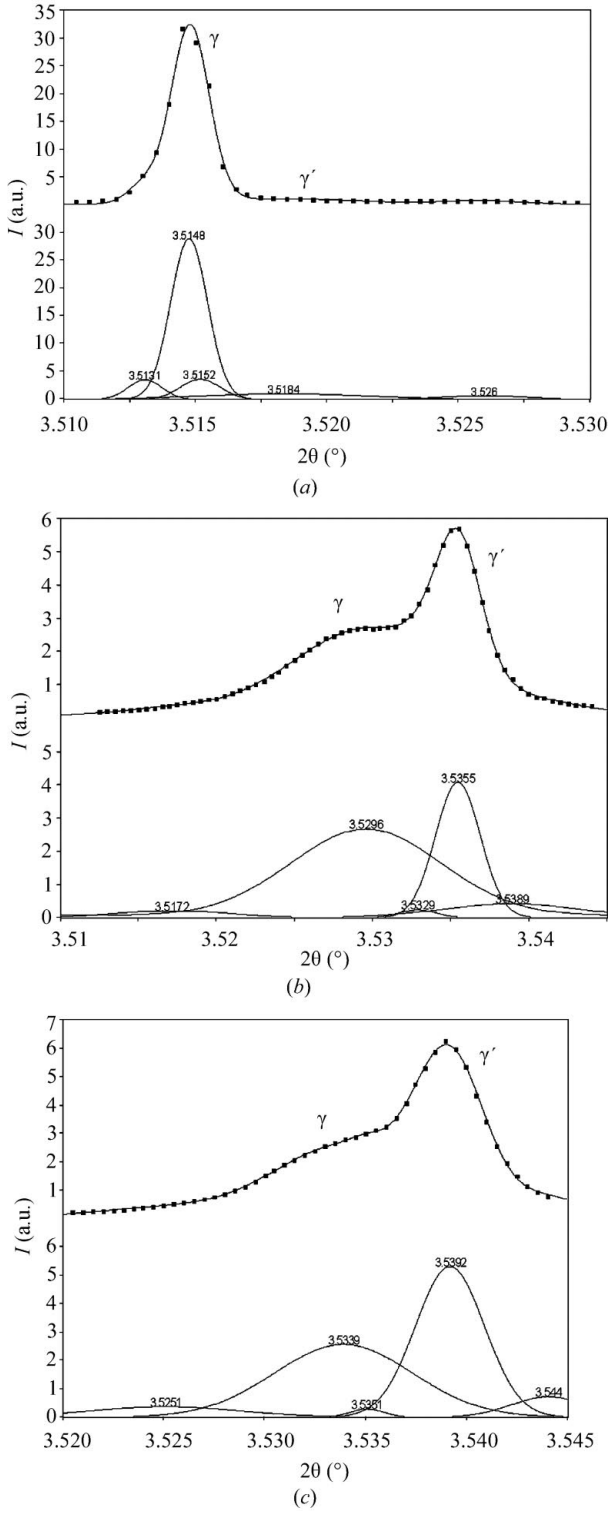


**Figure 3**
Typical peak shape at temperatures (*a*) $T = 1493$ K, (*b*) $T = 1373$ K and (*c*) $T = 1323$ K. Only the main peaks, labelled with $\gamma$ and $\gamma'$, were used for the determination of the misfit, but the fit has been performed using five or six peaks.

## 4. Discussion

At each temperature, after cooling from the solvus point, nucleation is expected to be the driving mechanism in the first stages. Nucleation is replaced slowly by growth and, after long times (say $t > 4$ h), by coarsening (Bruno & Pinto, 2003). Thus, at high temperatures ($T > 1373$ K), particles are born coherent and their mismatch is initially very low (the lowest compatible with the thermal expansion coefficients, CTEs, of the two phases). As time goes on, the $\gamma'$ particle size increases, and the misfit becomes larger (*i.e.* more negative). Below 1273 K, the relaxation gets slower, and at 1123 K the misfit is basically constant from the very early stages. This strongly supports the idea that newly nucleated particles drive the real-time evolution of $\delta$ and that the misfit depends essentially on the difference of CTE (Bruno, Schumacher *et al.*, 2003). Those results are also confirmed by neutron diffraction (Bruno & Pinto, 2003).

The asymptotic value of the misfit is reached once the nucleation has stopped being the predominant phenomenon, while diffusion is still active and coarsening takes place. This behaviour has been checked with long-term ageing at 1273 K (for 25 h and 100 h) and 1123 K (for 150 h). At these temperatures, a proliferation of the number of peaks was observed, which evolved with time. Therefore, a longer ageing time was selected during the kinetic study and more samples were prepared. The results for those additional samples are shown in Fig. 7. At 1273 K and after 25 h or 100 h, the misfit takes the same value as it had after 10 h of ageing. At 1123 K the misfit stays constant for 150 h. This result proves that diffusion, which for example tends to smear the dendritic structure, plays an eminent role

during nucleation only, and element partitioning between $\gamma$ and $\gamma'$ does not influence $\delta$, if element partitioning ever changes significantly. The behaviour of $\delta$ *versus* time $t$, at each temperature $T$, was fitted with an exponential decay. Two examples are given in Fig. 8. Although some points have a relatively large error, the behaviour of $\delta$ as a function of time is clearly recognizable, and the fit was weighted on the experimental errors. The half-life for relaxation is displayed in Table 2. The values obtained by neutron diffraction, as measured on the powder diffractometer E9 at the HMI, Berlin, Germany, are presented in parentheses. The small discrepancies between the two sets of results can be explained by means of the different temperature profile adopted [on E9 a cascade ladder-like profile was used (Bruno & Pinto, 2003)]. If we define the relaxation rate ($R_R$) as the inverse of the half-life, we find a behaviour of $R_R$ *versus* $T$ that has a maximum

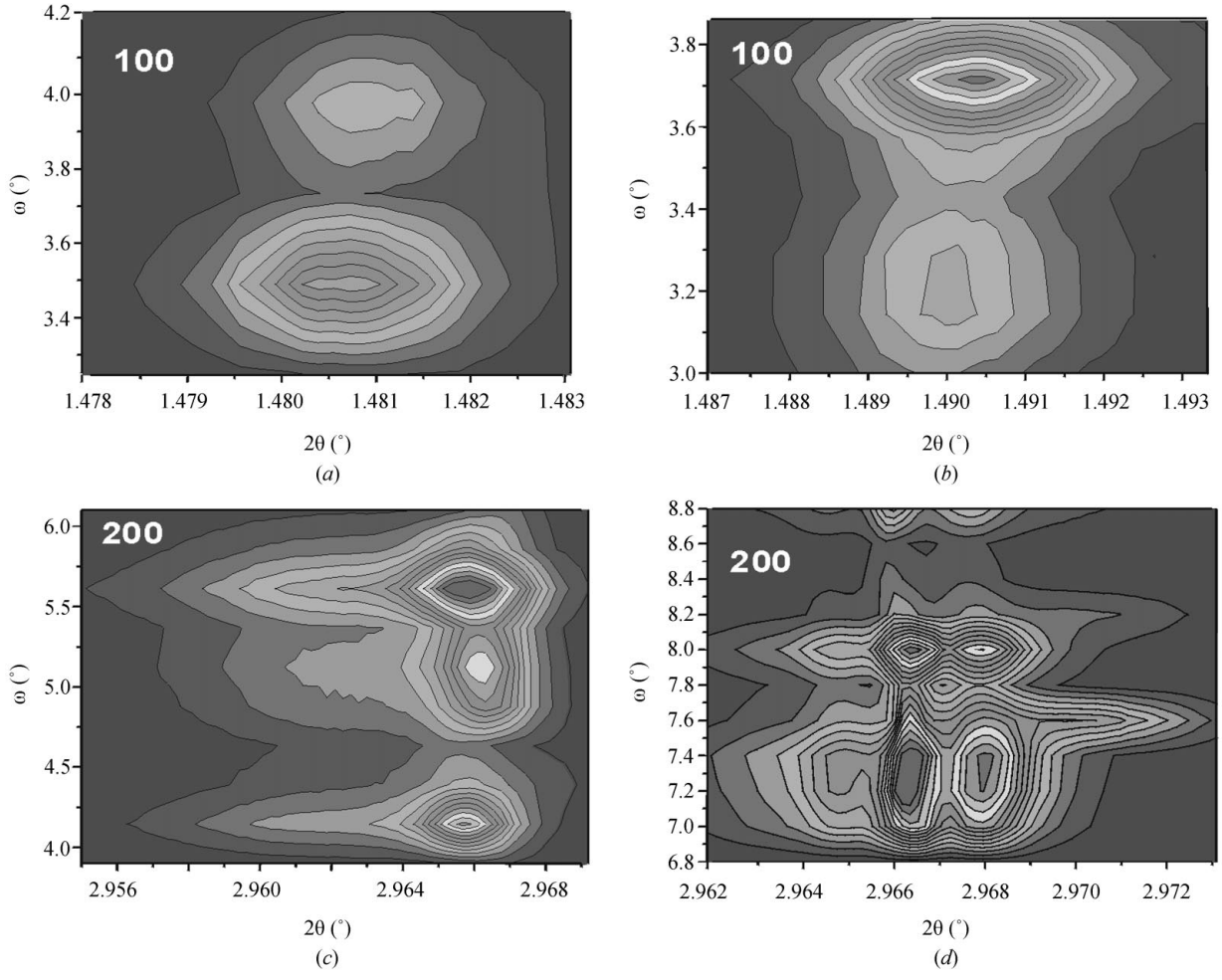


**Figure 4**
Contour plots at 1273 K and 1123 K, respectively, for the superstructure 100 reflection, (*a*) and (*b*), and for the fundamental 200 reflection, (*c*) and (*d*).

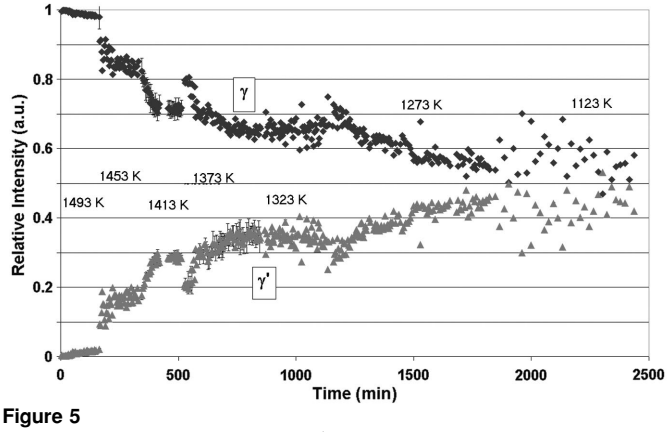


**Figure 5**
Integrated intensity of the $\gamma$ and $\gamma'$ main peaks as a function of time and temperature. The total intensity has been normalized to 1.

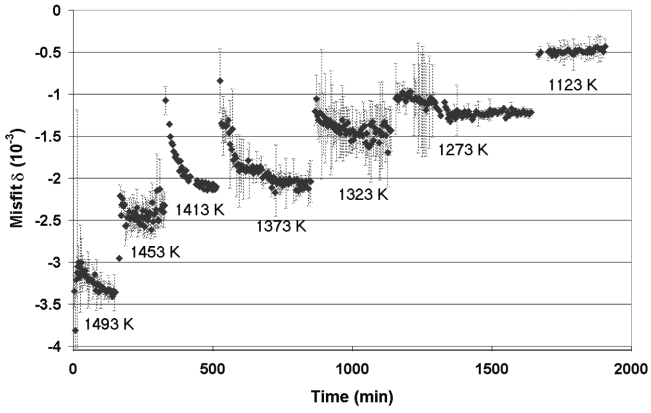


**Figure 6**
Lattice misfit as a function of time and temperature.

**Table 2**
Half-life and relaxation rate for the misfit $\delta$.

Values in parentheses were measured by neutron diffraction.

| $T$ (K) | $\tau$ (min) | $\Delta\tau$ (min) | $R_R$ (min$^{-1}$) | $\Delta R_R$ (min$^{-1}$) |
|---|---|---|---|---|
| 1493 | 80 | 6 | 0.0125 | 0.001 |
| 1453 | (45) | (9) | (0.023) | (0.0045) |
| 1413 | 39 (12) | 1 (8) | 0.0256 | 0.00016 |
| 1373 | 71 (30) | 7 (10) | 0.0141 | 0.0011 |
| 1323 | 55 | 14 | 0.0182 | 0.0046 |
| 1273 | 144 | 27 | 0.0069 | 0.0042 |
| 1123 | $\infty$ ($\infty$) | – | 0 (0) | – |

at around 1423 K (Table 2). Bruno & Pinto (2003) obtained a maximum of the total reaction rate at around 1323 K. This difference could result from the different natures of the reactions under examination. The misfit $\delta$ influences and represents only the $E_\delta$ (strain energy) contribution to the energy balance, while the integrated intensity comprises strain, interface and diffusion energies.

At each temperature, the coherency strains relax after 2–4 h, as the misfit $\delta$ reaches its final value. If coherency were lost only over longer times, the value of $\delta$ would also change during long-term ageing, whereas we found $\delta$ to be constant. This is confirmed by SEM images (Fig. 9), which show $\gamma'$ dendrites that are typical of a structure without coherency at interface (Durand-Charre, 1997).

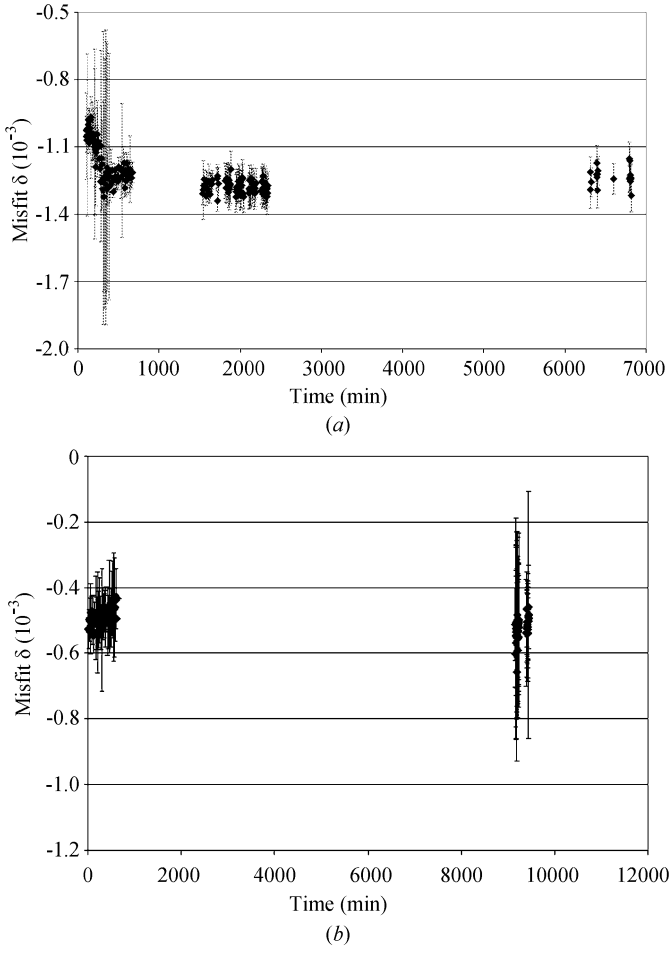


**Figure 7**
Behaviour of the misfit at 1273 K (*a*) and 1123 K (*b*), after long-time ageing. The value of $\delta$ remains constant, even after 150 h, at both temperatures.

The asymptotic values of the misfit at each temperature are displayed in Fig. 10. Here, the data obtained by Bruno, Schumacher *et al.* (2003), by heating an SHT sample from room temperature up to 1173 K, are also shown. A kind of hysteresis can be seen, and values of $\delta$ during cooling are always smaller. However, we note that

(i) the temperature where $\delta$ approaches 0 seems to be the same in both cases, *i.e.* about 773 K;

(ii) the microstructure of the alloy after SHT is much more 'regular' than that during any of the ageing treatments used in the cooling process (*i.e.* the arrangement is periodic and the shape is cuboidal rather than polyhedral, as indicated by Fig. 9).

Bruno, Schumacher *et al.* (2003) found that the lattice misfit of an SHT (or of an as-cast) sample depends mainly on the difference in the thermal expansion coefficient (CTE) of the two phases. The present results confirm and extend this conclusion.

The hysteresis can be explained if we assume that $E_\delta(T)$ is the same during both cooling and heating while the shape and the size (and their distributions) of the particles differ according to the process. In such a way $\delta$ can then have different values at the same temperature, if measured during heating or cooling, although the CTE difference must not depend on the process (heating or cooling).

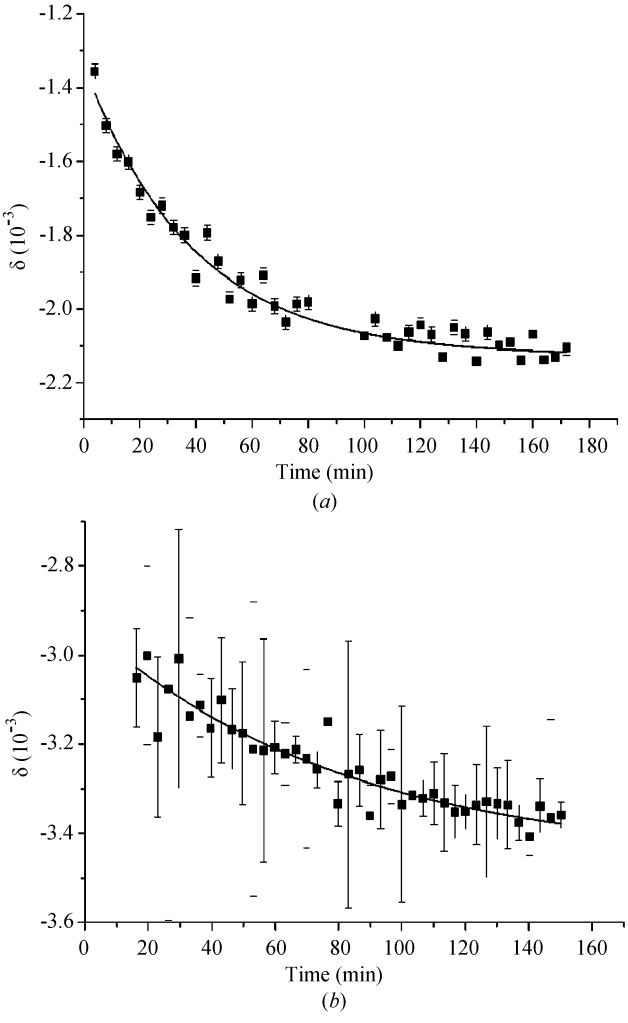


**Figure 8**
$\delta$ *versus* time at 1413 K (*a*) and 1493 K (*b*). The decay has been fitted with an exponential. Even if some error bars are rather large, the $r^2$ factor is near to 1, and the points lie very near to the fitting curve.

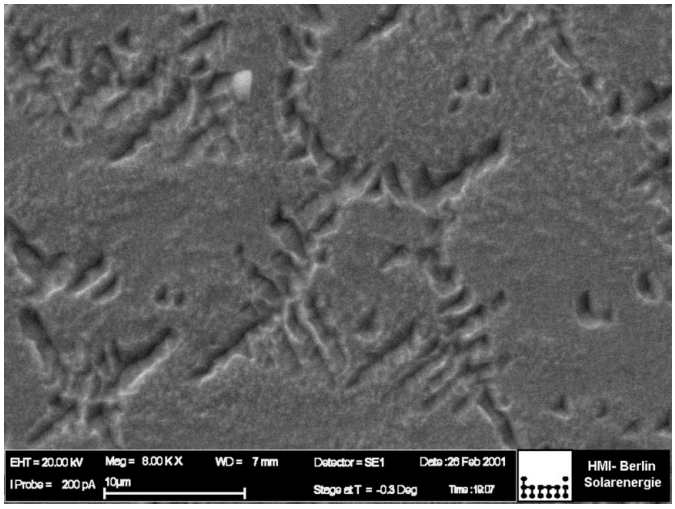


**Figure 9**
Scanning electron microscope image of $\gamma'$ dendrites for a sample treated at 1273 K.

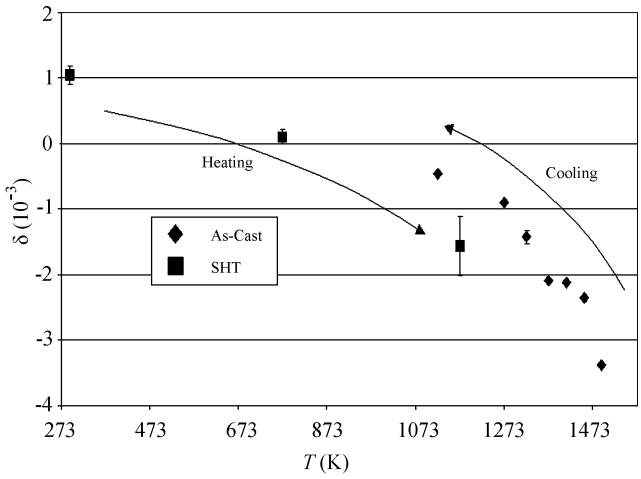


**Figure 10**
Behaviour of the misfit during cooling (this work) and heating (see Bruno, Schumacher *et al.*, 2003).

## 5. Conclusions

The real-time variation of the $\gamma$–$\gamma'$ lattice misfit was followed at several ageing temperatures at and below the solvus point ($T$ = 1523 K). A relaxation from a deformed coherent state to an incoherent and probably unstrained one was observed. The misfit decreases from a relatively low value (near $-1 \times 10^{-3}$ for most temperatures) to an asymptotic value that increases as the sample is cooled down. Longer ageing times did not change the value of the misfit, thus suggesting that (*a*) diffusional composition changes do not affect the value of $\delta$ as a function of time and (*b*) the reported loss of coherence takes place within 3 h at each temperature.

Point (*a*) is particularly important if we consider that the microstructure changes: the $\gamma'$ particles coarsen and the dendrites fade slowly. Point (*b*) underlines the fact that the misfit stays constant, as loss of coherence and strain relaxation compensate each other.

The relaxation rate has its maximum at around 1423 K. Therefore, at this temperature, the strain energy will play an eminent role during the early stages of nucleation. The influence of the strain energy will appear at later times during growth (for $T > 1423$ K) and even during coarsening (for $T < 1373$ K), *i.e.* it will be 'delayed' for relatively long times, since the characteristic times for misfit relaxation are longer than those found by Bruno & Pinto (2003) for the total nucleation and growth reaction.

A kind of hysteresis has been found in the heating/cooling cycle, as retrieved from present data and data extracted from (Bruno, Schumacher *et al.*, 2003). This hysteresis may be a result of $E_\delta(T)$ being the same regardless of the process [$E_\delta(T)$ depends only on the balance between shape and misfit effects], while $\delta(T)$ is also a function of the process underway. Therefore $E_\delta(T)$, rather than $\delta$ itself, strictly depends on the $\gamma$–$\gamma'$ CTE mismatch.

Hermann Franz and Martin von Zimmermann, HASYLAB, Hamburg, Germany, provided experimental help on the BW5 and Petra II beamlines and data interpretation support. Financial support from the Deutsche Forschungsgemeinschaft (DFG) is acknowledged (contract RE 688 35-1/2). This work has been presented at the TINX (Time-Resolved Investigations of Structural Changes in Soft and Solid Matter with Neutrons and X-rays) Workshop, held in Sommerfeld near Berlin, Germany, 4–6 September 2001.

## References

Bouchard, R., Hupfeld, D., Lippmann, T., Neuefeind, J., Neumann, H.-B., Poulsen, H. F., Rütt, U., Schmidt, T., Schneider, J. R., Süssenbach, J. & von Zimmermann, M. (1998). *J. Synchrotron Rad.* **5**, 90–101.
Bruno, G. & Cavalcanti Pinto, H. (2003). *Mater. Sci. Tech.* In the press.
Bruno, G., Cavalcanti Pinto, H., Strunz, P. & Wilhelm, M. (2003). In preparation.
Bruno, G., Schumacher, G., Cavalcanti Pinto, H. & Schulze, C. (2003). *Met. Trans.* **34**A, 193–197.
Durand-Charre, M. (1997). *The Microstructure of Superalloys.* Amsterdam: Gordon and Breach.
Fredholm, A. & Strudel, J. L. (1984). *Proceedings of the 5th International Symposium on Superalloys*, pp. 211–220. TMS AIME.
Gilles, R., Mukherji, D., Strunz, P., Wiedenmann, A. & Wahi, R. P. (1997). *Z. Metallkd*. **88**, 518–521.
Haasen, P. (1993). *Physical Metallurgy.* Cambridge University Press.
Hopgood, A. A. & Martin, J. W. (1986). *Mater. Sci. Tech.* **2**, 543–546.
Johnson, W. C., Abinadanan, T. A. & Voorhees, P. W. (1990). *Acta Metall. Mater.* **38**, 1349–1367.
Kampmann, R., Lippmann, T., Burmester, J., dos Santos, J. F., Franz, H., Haese-Seiller, M. & Marmotti, M. (2001). *Nucl. Instrum. Methods*, A**467**/**468**, 1261–1264.
Lorenz, G., Neder, R. B., Marxbreiter, J., Frey, F. & Schneider, J. (1993). *J. Appl. Cryst.* **26**, 632–635.
MacKay, R. A. & Nathal, M. V. (1986). *Am. Soc. Test. Mater. Spec. Tech. Publ.* **979**, 202.
Malow, T. (1993). Diplomarbeit, Technical University Berlin, Germany.
Malow, T., Zhu, J. & Wahi, R. P. (1994), *Z. Metallkd*. **85**, 9–19.
Royer, A., Bastie, P. & Veron, M. (1997). *Mater. Sci. Eng.* A**234**/**236**, 1110–1113.
Royer, A., Bastie, P. & Veron, M. (1998). *Acta Mater.* **46**, 5357–5368.
Rütt, U., Neumann, H. B., Poulsen, H. F. & Schneider, J. R. (1995). *J. Appl. Cryst.* **28**, 729–737.

 Received 21 December 2001 • Accepted 16 October 2002 